ELSEVIER

International Journal of Heat and Fluid Flow 22 (2001) 113–122

International Journal of HEAT AND FLUID FLOW

www.elsevier.com/locate/ijhff

Three-dimensional flow and heat transfer calculations of film cooling at the leading edge of a symmetrical turbine blade model

D. Lakehal [1], G.S. Theodoridis [2], W. Rodi *

Institute for Hydromechanics, University of Karlsruhe, Kaiserstrasse 12, D-76128 Karlsruhe, Germany

Received 28 October 1999; accepted 11 November 2000

Abstract

Film cooling of a symmetrical turbine-blade model by lateral and non-lateral injection from one row of holes placed on each side near the leading edge is calculated with a 3D finite-volume method on multi-block grids. For various blowing rates, the flow and temperature fields are predicted, and in particular the contours of film-cooling effectiveness on the blade surface, which are compared with measurements. Various versions of the k–ε turbulence model are employed: the standard model with wall functions (WF), a two-layer version resolving the viscous sublayer with a one-equation model and an anisotropy correction due to Bergeles et al. [Num. Heat Transfer 1 (1978) 217–242] which acts to promote the lateral turbulent exchange. The original Bergeles proposal is modified for application in the viscous sublayer. With the standard model, the lateral spreading of the temperature field is underpredicted, leading to averaged film-cooling effectiveness values that are too low. The situation is improved by using the Bergeles correction, especially when the modified correction is applied with the two-layer model (TLK). This yields effectiveness contours in reasonably good agreement with the measurements, but the laterally averaged effectiveness is not predicted in all cases with good accurary. However, the trend of the various influence parameters is reproduced correctly.

Keywords: Film cooling; Two-layer model; Turbine blade; Near-wall turbulence

1. Introduction

Increasing the turbine inlet temperature is one of the main measures for increasing the thermal performance of gas turbines. Despite the considerable progress in blade metallurgy, such temperature increases can only be afforded when the blades can be cooled efficiently. Film cooling is one of the most efficient cooling methods and is usually applied in combination with internal convection cooling. In film cooling, cool air is discharged from rows of holes placed in critical regions of the blade surface. The injected air forms a thin film on the surface acting as a buffer between the hot gas and the blade. The task of the blade designer is to achieve optimum cooling by a minimum amount of cooling air. The cooling performance is influenced by a variety of parameters, among them blade and discharge geometry, injection angle, blowing rate, density and temperature ratio, free stream turbulence, compressibility, and hence powerful prediction methods are needed for the optimisation of the design.

The flow in the vicinity of the film-cooling discharge holes is very complex due to the interaction of the discharge jets with the flow around the blade. The individual jets are bent over by the oncoming flow leading to the formation of longitudinal vortices and a reverse-flow region below the jet. The flow is highly 3D and turbulent, and it becomes even more complicated when the injection is lateral which is often the case in practice since then the cooling film covers better the area to be cooled. Injection near the leading edge causes further complications as the cooled jets are then opposed to the oncoming flow, but this injection location is of particular practical relevance because the leading edge is exposed especially to the oncoming hot gases. The formation and location of the longitudinal vortices depend strongly on the inclination of the injection and on the blowing rate $M(=\rho_2 U_2/\rho_\infty U_\infty$, also called mass-flux ratio). In the case of streamwise injection, two counter-rotating vortices form while in the case of lateral injection there is only one large-scale vortex. The vortices entrain ambient hot gas and move it to the vicinity of the wall and hence adversely influence the film-cooling effectiveness. This phenomenon is more pronounced at higher blowing rates for

* Corresponding author. Tel.: +49-721-608-3535; fax: +49-721-608-7712 or 7290.

E-mail address: rodi@bau-verm.uni-karlsruhe.de (W. Rodi).

[1] Present address: Nuclear Engineering Laboratory, Institute of Energy Technology, ETH Zürich, CH-8092 Zürich, Switzerland.

[2] Present address: Department of Mechanical and Industrial Engineering, University of Thessaly, Pedion Areos, GR-38334, Volos, Greece.

0142-727X/01/$ - see front matter
PII: S0142-727X(00)00084-9

Notation

C's	constants in turbulence model
C_ℓ	model constant in Eq. (9) $= \kappa C_\mu^{-3/4}$
C_p	specific heat under constant pressure
D	discharge pipe diameter
E	roughness parameter
f	near-wall anisotropy correction factor
f_μ	damping function defined in Eq. (9)
h	enthalpy ($\Delta h \equiv C_p \Delta T$)
k	turbulent kinetic energy
M	blowing rate $= (\rho_2 U_2)/(\rho_\infty U_\infty)$
Pr	molecular Prandtl number
P_k	turbulence production
s	lateral hole spacing, length along blade from stagnation point
T	temperature
Tu	free-stream turbulence level
U_i	Cartesian velocity components $= U, V, W$
x_i	Cartesian coordinates $= x, y, z$
y_n	Distance to the wall
y^+	dimensionless wall distance $= y_n U_\tau / \nu$

Greeks

A_μ	one-equation model constant
C_μ	model constant in Eq. (3)
δ	boundary layer thickness
η	film-cooling effectiveness $= (T_w - T_\infty)/(T_2 - T_\infty)$
$\overline{\eta}$	laterally averaged film-cooling effectiveness
ϵ	dissipation rate of turbulent kinetic energy
Γ's	diffusion coefficients
γ	pipe-inclination angle $= 0°$ or $45°$
κ	Von Kármán constant
ℓ_μ	Turbulent length–scale in Eq. (8)
ℓ_ε	dissipation scale
μ	molecular viscosity
μ_t	isotropic turbulent viscosity
μ_t^a	anisotropic turbulent viscosity
ν	kinematic viscosity
ρ	density
σ's	turbulent diffusion coefficients
σ_h	turbulent Prandtl number
τ_w	wall friction
U_τ	friction velocity $= \sqrt{\tau_w/\rho}$

Subscripts

∞	freestream
s	oncoming flow
w	wall
1	wall-neighbouring cell
2	coolant jet

which the jets penetrate more into the oncoming flow and the vortices are lifted further from the surface. The influence of the blowing rate M on the cooling effectiveness was discussed extensively in the literature. For low blowing rates the laterally averaged effectiveness decreases monotonically downstream while for high blowing rates it drops sharply behind the injection hole and then increases over quite some distance due to the high cooling mass flow (Haslinger and Hennecke, 1997). The lateral hole spacing s/D also has a significant influence. According to Ligrani et al. (1994) jet penetration into the main stream increases with increasing s/D due to the interaction of neighbouring jets, consequently lowering the averaged effectiveness. Only recently has detailed information become available on the behaviour of the flow and temperature fields around inclined film-cooling jets, but most experiments were carried out for flat-plate situations (Honami et al., 1992; Kohli and Bogart, 1995; Findlay et al., 1999) and only a few for blade models (Haslinger and Hennecke, 1997; Ardey, 1998).

The paper reports on research whose aim was the development of a 3D method for calculating the flow and heat transfer of film-cooling situations on turbine blades with lateral injection near the leading edge. Most previous computational works concern the investigation of film cooling of a flat plate, and the present authors have tested their method for this simple case first (Lakehal et al., 1998). There are only few 3D calculations of film cooling on turbine blade models: Garg and co-workers (Garg and Ameri, 1997; Garg, 1999; Garg and Rigby, 1999) report on calculations for various blades using the Baldwin–Lomax model and various two-equation turbulence models and studied the effect of a number of parameters on the flow and temperature field. Most of these calculations did not extend to the discharge channel while such an extension is really necessary, at least for low blowing rates, as was also concluded by Garg and Rigby (1999) in their survey paper. There was no clear picture emerging from the calculations on which turbulence model is superior. He et al. (1995) and Martin and Thole (1997) performed calculations for the situation of a semi-circular leading edge with several rows of cooling holes. In some of the cited studies for blade models, heat transfer was calculated but not the adiabatic film-cooling effectiveness. Recently, Ardey (1998) measured the flow fields around the leading edge of the so-called AGTB high-pressure turbine blade with shower-head injection. Calculations of this case without heat transfer are reported in Vogel (1996) and Bohn et al. (1997) and in a companion paper of the authors (Theodoridis et al., 2000). Film-cooling effectiveness was measured on a symmetrical model of the AGTB blade in a related project at the University of Darmstadt (Haslinger and Hennecke, 1997), and in the present work the 3D film-cooling method is tested and developed further by application to this particular situation.

Previous calculations, including those of Lakehal et al. (1998), of film-cooling jets have shown that standard two-equation models like the k–ε model with wall functions (WF) are not very adequate for the complex flows considered and especially not for predicting the heat transfer; in particular the lateral spreading of the temperature field was found to be underpredicted. Resolving the near-wall region in the calculations was seen to lead to an improvement, and the calculations of Lakehal et al. (1998) with the two-layer model (TLK) of Rodi (1991) indeed met with some success: hence this approach was followed here also. Another measure to improve the lateral spreading is to replace the isotropic eddy viscosity/diffusivity used in the original models by an anisotropy model suggested by Bergeles et al. (1978). This was also adopted and tested in the present work and it was extended for application very near the wall in connection with the TLK.

2. Mean-flow equations and turbulence model

The 3D, steady, incompressible turbulent mean flow and temperature fields are governed by mass conservation ($\partial U_i/\partial x_i = 0$), and momentum and enthalpy transport equations which can be expressed in terms of Cartesian tensor notation in the following compact form:

$$\frac{\partial}{\partial x_j}\left[\rho U_i U_j - \Gamma_u\left(\frac{\partial U_i}{\partial x_j}+\frac{\partial U_j}{\partial x_i}\right)\right] = -\frac{\partial p}{\partial x_i}, \tag{1}$$

$$\frac{\partial}{\partial x_j}\left[\rho U_j h - \Gamma_h \frac{\partial h}{\partial x_j}\right] = 0, \tag{2}$$

where the velocity components U_i and the enthalpy $h = C_p T$ for the temperature-determining equation are time-averaged variables (C_p = specific heat), p the pressure and ρ is the fluid density. The turbulent stresses $\overline{u_i' u_j'}$ and heat fluxes $\overline{u_i' h'}$ appearing in the original momentum and enthalpy equations have been replaced in (1) and (2) by relations involving the mean-velocity and temperature gradients with the aid of the eddy-viscosity/diffusivity concept. Hence, the momentum diffusion and thermal diffusion coefficients read, respectively, $\Gamma_u = (\mu + \mu_t)$ and $\Gamma_h = (\mu/Pr + \mu_t/\sigma_h)$. Here μ and μ_t designate the molecular and turbulent (or eddy) viscosities, respectively, and Pr and σ_h are the corresponding molecular and turbulent Prandtl numbers. The distribution of the eddy viscosity over the flow field has to be calculated with the aid of a turbulence model and the value of the turbulent Prandtl number σ_h also has to be specified by this model.

2.1. k–ε Turbulence model

The distribution of the eddy viscosity μ_t is calculated with two versions of the k–ε turbulence model, namely the standard version of Launder and Spalding (1974), which bridges the viscous sublayer with the aid of WFs, and the two-layer version (Rodi, 1991) in which the viscous sublayer is resolved by a one-equation turbulence model. In the k–ε model, the eddy viscosity μ_t is related to the turbulent kinetic energy k and the rate of its dissipation ε by

$$\mu_t = C_\mu \rho k^2/\varepsilon \tag{3}$$

and the distribution over the flow field of the turbulence parameters k and ε is calculated from the following semi-empirical model transport equations:

$$\frac{\partial}{\partial x_j}\left(\rho U_j k - \Gamma_k \frac{\partial k}{\partial x_j}\right) = \underbrace{\mu_t\left(\frac{\partial U_i}{\partial x_j}+\frac{\partial U_j}{\partial x_i}\right)\frac{\partial U_i}{\partial x_j}}_{P_k} - \rho\varepsilon, \tag{4}$$

$$\frac{\partial}{\partial x_j}\left(\rho U_j \varepsilon - \Gamma_\varepsilon \frac{\partial \varepsilon}{\partial x_j}\right) = C_{\varepsilon 1} P_k \frac{\varepsilon}{k} - C_{\varepsilon 2}\frac{\rho\varepsilon^2}{k} \tag{5}$$

with $\Gamma_k = (\mu + \mu_t/\sigma_k)$ and $\Gamma_\varepsilon = (\mu + \mu_t/\sigma_\epsilon)$.

The laminar and turbulent Prandtl numbers Pr and σ_h appearing in the enthalpy equations are set to the values 0.7 and 0.9, respectively.

2.2. Standard model version

In the standard version, which is applicable only outside the near-wall region in which direct viscous effects are important, μ in Γ_k and Γ_ε can be neglected. Further, the standard values of the empirical constants are employed, namely: $C_\mu = 0.09$, $C_{\varepsilon 1} = 1.44$, $C_{\varepsilon 2} = 1.92$, $\sigma_k = 1$ and $\sigma_\varepsilon = 1.3$. When this version is used, the viscosity-affected near-wall region is not resolved but the first grid point is placed outside the viscous sublayer in a region where the dimensionless wall distance $y^+ = yU_\tau/\nu$ has a value of 30–100, in any case $y^+ > 11$. For attached boundary layers, in this region the universal log law is valid and turbulence is approximately in local equilibrium (production = dissipation). The velocity U_{res} parallel to the wall as well as k and ε at the first grid point are then calculated by relating them via the following WFs to the wall shear stress τ_w (with $U_\tau = \sqrt{\tau_w/\rho}$):

$$\frac{U_{res}}{U_\tau} = \frac{1}{\kappa}\ln\left(\frac{y_1 U_\tau}{\nu}E\right), \tag{6}$$

$$\frac{k}{U_\tau^2} = \frac{1}{\sqrt{C_\mu}}, \quad \varepsilon = \frac{U_\tau^3}{\kappa y_1}, \tag{7}$$

where y_1 is the distance of the first grid point from the wall, κ the von Kármán constant (= 0.41) and E is a roughness parameter (here $E = 9.0$ for smooth walls).

2.3. Two-layer version

In the two-layer approach, the viscosity-affected regions close to walls are now resolved with a one-equation model, while the outer core flow is calculated with the standard k–ε model described above. In the one-equation model, the ε-equation is not solved but the distribution of the turbulent length scales is prescribed empirically. Following Rodi (1991), the one-equation model of Norris and Reynolds (1975) is used. This calculates the eddy viscosity from

$$\mu_t = C_\mu \rho k^{1/2} l_\mu, \tag{8}$$

where k is determined from the k-equation (4) (now with μ in Γ_k). The length scale l_μ is given by the following empirical relation:

$$l_\mu = c_l y_n \underbrace{\left[1 - \exp\left(-\frac{R_y}{A_\mu}\right)\right]}_{f_\mu}, \tag{9}$$

where y_n is the local distance normal to the wall and f_μ is a damping function similar to the van Driest damping function in the Prandtl mixing-length model. However, in the local Reynolds number $R_y = y_n k^{1/2}/\nu$, the turbulent energy $k^{1/2}$ is used as the velocity scale instead of the friction velocity U_τ in the original van Driest function which can go to zero in separated flows. The constant c_l is set equal to $\kappa C_\mu^{-3/4}$ to conform with the logarithmic law of the wall, and the empirical constant A_μ is given the value $A_\mu = 50.5$. ε in the k-equation (4) is determined from

$$\varepsilon = \frac{k^{3/2}}{l_\varepsilon} \quad \text{with the length scale } l_\varepsilon \text{ from}$$

$$l_\varepsilon = \frac{c_l y_n}{1 + 13.2/(R_y c_l)}. \tag{10}$$

The k–ε-model for the outer region and the near-wall one-equation model are matched dynamically (with no fixed zones) at a location where the damping function f_μ reaches the value 0.95, i.e., where viscous effects become negligible.

2.4. Modified anisotropy correction due to Bergeles et al. (1978)

The models introduced so far use an isotropic eddy viscosity/diffusivity, i.e., the exchange coefficients for the turbulent transport are assumed to be the same for all directions. However, previous film-cooling and jet-in-a-cross-flow calculations have revealed consistently that with such a model the film-cooling jets do not spread sufficiently in the lateral direction compared with experimental observations. From this it can be concluded that with an isotropic eddy-viscosity/diffusivity model, the turbulent transport in the lateral direction is not accounted for sufficiently and that in reality the eddy viscosity/diffusivity for transport in this direction should be larger than for the transport normal to the wall. This is supported by the recent measurements of Ardey (1998) who found that in

the vicinity of film-cooling injections the lateral turbulent fluctuations $\overline{w'^2}$ are generally larger than the normal fluctuations $\overline{v'^2}$. In order to account for the anisotropy of the turbulent exchange processes in these flows and to enhance the lateral turbulent transport, Bergeles et al. (1978) proposed to substitute the eddy viscosity μ_t appearing in the lateral components of the Reynolds stresses and heat fluxes:

$$-\rho\overline{u'w'} = \mu_t \frac{\partial U}{\partial z}, \quad -\rho\overline{w'T'} = \frac{\mu_t}{\sigma_h}\frac{\partial T}{\partial z} \tag{11}$$

by an increased value determined by

$$\mu_t^a = \mu_t[1.0 + f(1.0 - y/\delta)], \tag{12}$$

in which μ_t is the eddy viscosity determined by the basic turbulence model as described above. δ denotes the local boundary-layer thickness. Eq. (12) was derived from model transport equations for the Reynolds stresses by assuming the local equilibrium of turbulence and neglecting the stresses $\overline{v'w'}$ against $\overline{u'v'}$ and $\overline{u'w'}$. The ratio of eddy viscosities/diffusivities for the stresses and heat fluxes in the lateral and normal directions was then found to be equal to the ratio of the fluctuating velocities $\overline{w'^2}/\overline{v'^2}$, which was assumed to vary linearly from a near-wall value $f + 1$ to unity at the outer edge of the boundary layer. For the near-wall region, in which the logarithmic velocity profile prevails (outside the viscous sublayer), Bergeles et al. derived from measurements a value of $f = 3.5$. This anisotropy eddy-viscosity correction was already employed by Demuren et al. (1985) and recently by Zhou et al. (1993) for the prediction of 3D turbulent jets in cross flow, but limiting its implementation to the lateral components of the Reynolds stresses and heat fluxes in the mean-flow equations. In the present study, implementation of the correction was extended to all transport equations, and in particular to the diffusion and turbulence production terms appearing in the transport equations for k and ε. The original correction with $f = 3.5$ was used in connection with the standard k–ε model with WFs, but in most calculations the anisotropy was increased further by putting $f = 8.0$.

Since the normal fluctuations $\overline{v'^2}$ approach zero near the wall much faster than the lateral fluctuations $\overline{w'^2}$, the ratio $\overline{w'^2}/\overline{v'^2}$ reaches much larger values in the viscous sublayer than the value of 4.5 adopted in the original model at the edge of the sublayer. This must be accounted for when the anisotropy correction is used together with a model resolving the viscosity-affected near-wall region, such as the TLK. A relation for the near-wall behaviour of $\overline{w'^2}/\overline{v'^2}$ was therefore derived in this study from direct numerical simulation (DNS) data of Kim for channel flow as reported in Rodi et al. (1993) and also in the AGARD Advisory Report 245 (1998). The DNS calculations for the ratio $\overline{w'^2}/\overline{v'^2}$ were approximated by the following empirical relation:

$$\frac{\overline{w'^2}}{\overline{v'^2}} = \frac{10^3(y^+)^{0.42}}{2.682(y^+)^2 - 5.463}, \tag{13}$$

where y^+ is the non-dimensional wall distance $y^+ = U_\tau y/\nu$, with U_τ being the friction velocity. Since the dependence on y^+ is not suitable for separated flows, this parameter is replaced by a dimensionless wall distance $R_y = k^{1/2}y_n/\nu$. The relation between y^+ and R_y also follows from the DNS channel flow data, from which the following correlation is derived:

$$R_y = 0.00442(y^+)^2 + 0.294y^+ + 0.545. \tag{14}$$

Relation (13) shows that very near the wall the anisotropy grows drastically so that $\mu_t^a/\mu_t = \overline{w'^2}/\overline{v'^2}$ reaches very high values. In the model, the maximum was limited to 60. From a wall distance where (13) yields a value of 4.5, μ_t^a/μ_t is then calculated again from (12), with $f = 3.5$.

3. Outline of the computational procedure

For the calculation of the flow around a model turbine blade considered here, the equations are written in curvilinear coordinates as given in Lakehal et al. (1998). These equations are solved with a 3D finite-volume method that allows to use arbitrary non-orthogonal grids, employing a cell-centred grid arrangement. A detailed description of the method is reported in Majumdar et al. (1992), and the multi-block technique which was introduced afterwards, in Rodi et al. (1997) and Lakehal et al. (1998). The momentum-interpolation technique of Rhie and Chow (1983) is used to prevent the pressure-field oscillations which tend to appear in the cell-centred grid arrangement. The pressure–velocity coupling is achieved using the SIMPLEC algorithm of Van Doormal and Raithby (1984). The computations with the standard k–ε and the TLKs were performed employing the second-order oscillation-free *Hybrid Linear Parabolic Approximation* scheme (HLPA) developed by Zhu (1991) to approximate the convection fluxes of all variables. The resulting system of difference equations was solved using the (SIP) algorithm of Stone (1968).

4. Test case, grids and boundary conditions

4.1. Test case description

The turbine blade model considered in this work has been studied experimentally at the Technical University of Darmstadt, Germany, and detailed information on the experiments is available in Haslinger and Hennecke (1997). The blade model is symmetrical with a length of 515 mm and a maximum width of 72 mm. The leading part of the outer model shape is identical to the scaled suction side of a high-pressure turbine blade called AGTB. The leading edge of the model contains on each side one row of holes ($D = 4$ mm) with a lateral spacing of $5D$. The geometry is shown in Fig. 1. Two configurations with different lateral inclinations of the injection channels were investigated: one without lateral inclination ($\gamma = 0°$, streamwise injection) and one with a lateral inclination of $\gamma = 45°$ (lateral injection). The approach-flow velocities were in the range $U_\infty = 15$–30 m/s so that the flow can be considered incompressible. The free-stream turbulence level was below 0.5%. Calculations were carried out only for the approach velocity of 30 m/s corresponding to a Reynolds number (based on injection-hole diameter D and approach velocity) of 7950. Seven mass-flux ratios $M = \rho_2 U_2/\rho_\infty U_\infty = 0.3$, 0.5, 0.7, 0.9, 1.1, 1.3 and 1.5 (U_2 and ρ_2 are, respectively, the injected jet velocity and density and ρ_∞ is the primary stream density) were investigated in the experiment. Mainly the distributions of the adiabatic film-cooling effectiveness were measured with an

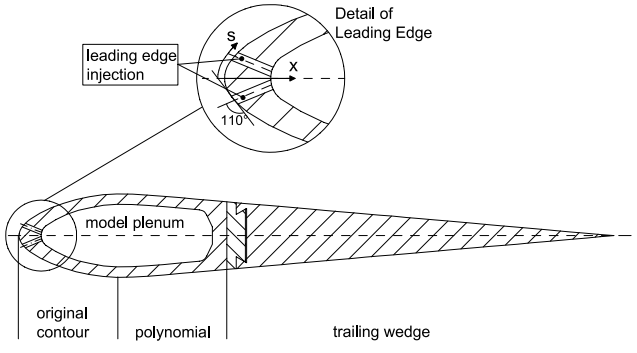

Fig. 1. Model blade geometry (from Haslinger and Hennecke, 1997).

Ammonia and Diazo technique with CO_2 calibration and some flow visualisations by injecting an air/oil-fog mixture were conducted in planes parallel and perpendicular to the cooling jets. In addition, the pressure distribution around the blade was measured.

4.2. Grids and boundary conditions

Owing to the symmetry of the problem, only half of the flow domain of interest needs to be calculated so that the upper boundary consists of half the blade surface and symmetry planes upstream and downstream of the blade. The lower boundary is placed 180 mm below the symmetry plane at the location of the wind-tunnel wall, where WFs were used in all calculations. The inflow boundary is located 360 mm upstream of the leading edge and and the outflow boundary 385 mm downstream of the trailing edge.

In the case of streamwise injection ($\gamma = 0°$), the calculation domain extends from a plane through the middle of the holes ($z = 0$) to a plane at $z/D = 2.5$ in the middle between two injection holes, and symmetry conditions are imposed on these planes. A multi-block grid is used consisting of three blocks, one block in the front part up to the injection, one block in the external region downstream of the injection and one block inside the injection channel (see Fig. 2). Preliminary calculations with WFs were performed on different grids with $126 \times 54 \times 14$, $152 \times 68 \times 16$ and $178 \times 75 \times 19$ points in the x, y and z directions, respectively. The first grid proved to be rather coarse while the results with the second and third grids were nearly identical. Hence the $152 \times 68 \times 16$ grid was adopted. When the TLK was applied $226 \times 88 \times 34$ grid points were used and no further grid refinement was possible. In the wall-function calculations the injection channel, which has a length of $5D$, was discretised with $16 \times 8 \times 6$ points and in the case with near-wall resolution by $28 \times 26 \times 14$ points. The fine grid has approximately 700,000 grid points.

In the case of lateral injection ($\gamma = 45°$), the calculation domain lies between the planes $z/D = -2.5$ and +2.5, i.e., between the two planes placed in the middle between the adjacent holes on either side. Periodic boundary conditions are imposed there. Since the lateral extent of the calculation domain is twice as large as in the case with non-lateral injection, more grid points are needed in the lateral direction. Hence for calculations with WFs altogether $152 \times 68 \times 34$ points were placed in the x-, y- and z-direction and when the TLK was applied $180 \times 80 \times 56$ grid points. The injection channel was discretised in the former case by $16 \times 8 \times 12$ grid points and in the latter case with near-wall resolution by $28 \times 20 \times 20$ grid points. It should be mentioned that the grids were refined considerably in the vicinity of the injection hole. When the TLK was used, the size of the first grid cell was set to a value which conforms to y^+ being in the range 0.3–3.

On the wall surface of the blade, the boundary conditions described above for the different turbulence models were used (WFs for the standard model, no-slip conditions for the TLK). As mentioned already, on the lower wind-tunnel wall, WFs were used in all calculations. At the inflow boundary, a uniform streamwise velocity profile was applied ($U_s = 30$ m/s). Uniform distributions were also specified for k and ε corresponding to a free-stream turbulence intensity of $Tu = 0.5\%$ and a dimensionless eddy viscosity of $\mu_t/\mu = 30$. Similarly, a uniform velocity profile was set at the inlet of the discharge pipe ($U_2 = M \times U_\infty$). Here also, uniform distributions of k and ε were specified, based on a turbulence intensity of $Tu = 3\%$ and a length scale of $k^{3/2}/\varepsilon = 0.3D$. Adiabatic wall conditions were employed when solving the enthalpy equation; zero gradient conditions were used at the outflow boundary.

5. Results and discussion

2D calculations of the flow around the blade model were first carried out without injection, using a medium fine 127×29 grid and a fine 187×47 grid. The pressure distribution around the blade calculated with these two grids did not differ significantly and agreed very well with the measured pressure distribution (see Rodi et al., 1997). The calculations were carried out with the standard k–ε model with WFs while in the experiment the boundary layer without injection remained laminar in the front part. The fact that there is still good agreement between calculations and measurements indicates that the boundary layer in this part is very thin and has negligible influence on the pressure distribution around the blade.

5.1. Streamwise injection ($\gamma = 0°$)

Calculations with the standard k–ε model with WFs were carried out for the blowing rates $M = 0.3$, 0.5 and 0.9. The velocity vectors predicted for $M = 0.3$ and 0.9 in the mid-plane

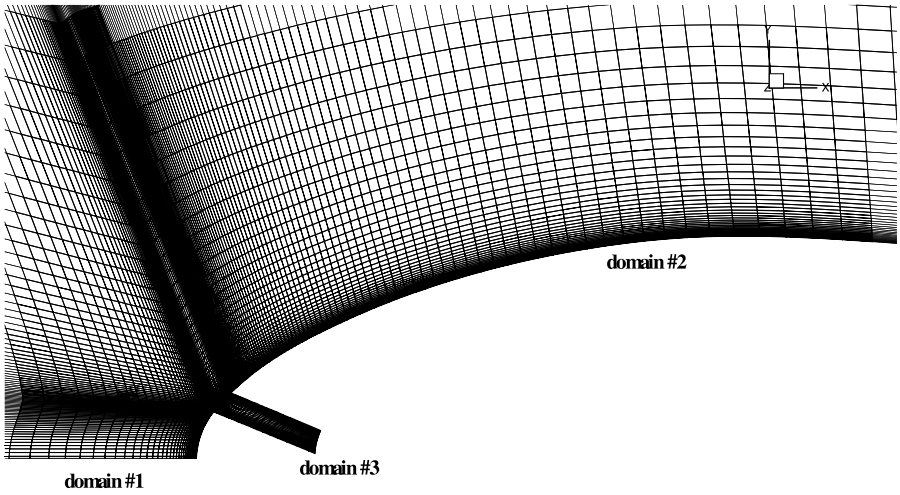

Fig. 2. Grid for calculations with streamwise injection ($\gamma = 0°$) using the two-layer model.

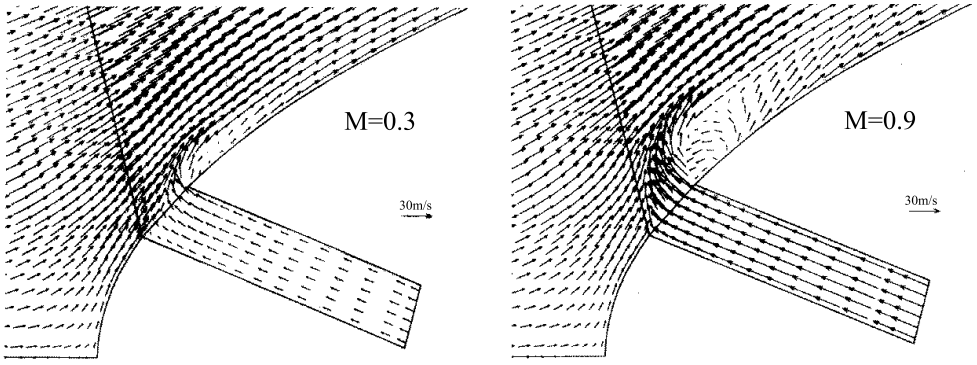

Fig. 3. Calculated velocity vectors in mid-plane through the injection hole for streamwise injection ($\gamma = 0°$); calculations with the standard k–ε model and wall functions.

of the hole are displayed in Fig. 3. They show the flow around the leading edge of the blade and the interaction of the injected jet with the outer flow. At $M = 0.3$ the jet is bent over strongly to the right after the injection and only a small zone with low or reverse-flow velocities is formed. This zone increases as the blowing rate is increased. At $M = 0.9$ the reverse-flow region has an extent of about one hole diameter downstream of the trailing edge of the injection hole. However, there is no direct recirculation as the fluid flowing in the upstream direction enters laterally into the reverse-flow region. In Fig. 4, the corresponding velocity vectors predicted with the TLK with extended Bergeles correction are presented for $M = 0.9$. Basically similar behaviour can be observed, but the resolution is of course much better than when WFs are used so that more details of the flow pattern appear compared with Fig. 3. The increased resolution also led to the development of a small recirculation zone right behind the leading edge of the discharge hole. Further, compared with the calculations for WFs, the reverse-flow region is now larger, extending to about $1.1D$ from the injection hole trailing edge, and the details of the flow in the interaction region are altogether more complex.

Fig. 5 compares the calculated contours of the film-cooling effectiveness $\eta = (T_w - T_\infty)/(T_2 - T_\infty)$ on the blade surface with the measurements for the blowing rates $M = 0.3$, 0.5 and 0.9. Here T_w, T_∞ and T_2 are, respectively, the wall, free-stream and cooling gas temperature. In this and in the following figures on film-cooling effectiveness the abscissa s is the length measured along the blade surface from the stagnation point (see Fig. 1). The left part of the figure gives results for $M = 0.3$ obtained with various model versions and at the bottom for $M = 0.5$ obtained with the TLK and the extended Bergeles correction while in the right part of the figure results are displayed for $M = 0.9$ as obtained with various model versions. The top two panels of Fig. 5 show results obtained with the standard model with WFs and without Bergeles correction. For both blowing rates $M = 0.3$ and 0.9, this model clearly predicts too small lateral spreading of the temperature field and too small decay of the cooling effectiveness in the core region downstream of the injection. When the Bergeles correction is switched on for $M = 0.9$, here with a correction factor $f = 8$, the lateral spreading is now roughly correct and so is the near-field behaviour, but further downstream the decay of effectiveness is still too small near the injection jet axis. Using the TLK but without Bergeles correction ($f = 0$) has some positive effect in the case of $M = 0.3$ but leads to an even slower decay of the film cooling effectiveness for $M = 0.9$ and altogether does not increase the lateral spreading very much. Switching on in addition the extended Bergeles correction ($f = h(y^+)$) improves the overall predictions significantly. For the blowing rates calculated with this model ($M = 0.3$, 0.5, 0.9) the lateral spreading of the temperature field now corresponds roughly to the experimentally observed one and the decay of the effectiveness is now larger and hence closer to reality. It should be mentioned here that the contours in the downstream region are very sensitive to the values of η and hence the deviations are generally in the range of the measurement accuracy. However, for $M = 0.3$ the η-values in the experiments have a higher level over a wider lateral range so that the laterally averaged η-values are predicted altogether to be too low as shown in Fig. 6.

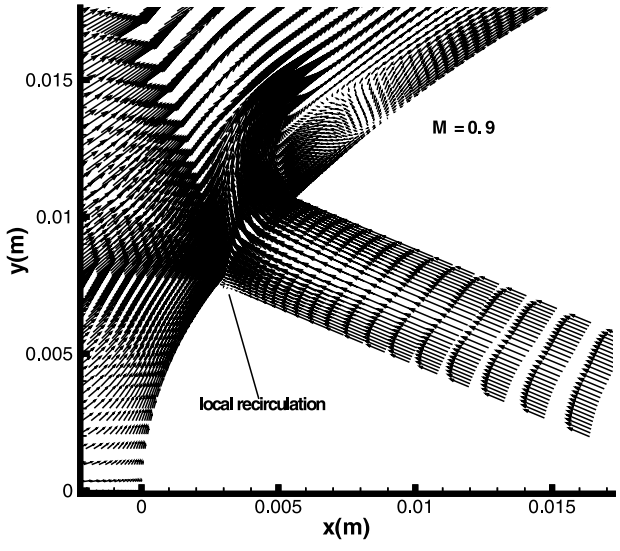

Fig. 4. Calculated velocity vectors in mid-plane through the injection hole for streamwise injection ($\gamma = 0°$); calculations with the TLK model ($f = h(y^+)$).

In Fig. 6, the laterally averaged film cooling effectiveness $\overline{\eta}$ is displayed as a function of the downstream distance; in Fig. 6(a) results are given for $M = 0.9$ as obtained with various turbulence-model versions. Using the standard model without Bergeles correction (WF, $f = 0$), $\overline{\eta}$ is generally predicted to be too low but too high very close to the injection; when the Bergeles correction is used with a factor $f = 8$, the $\overline{\eta}$-level further downstream agrees with the measured values, but it is even more overpredicted near the discharge hole as was to be expected from the wider predicted contours in this region shown in Fig. 5. The calculations with the TLK and extended Bergeles correction yield for $M = 0.9$ a fairly good agreement with the measurements over the whole range. The relatively

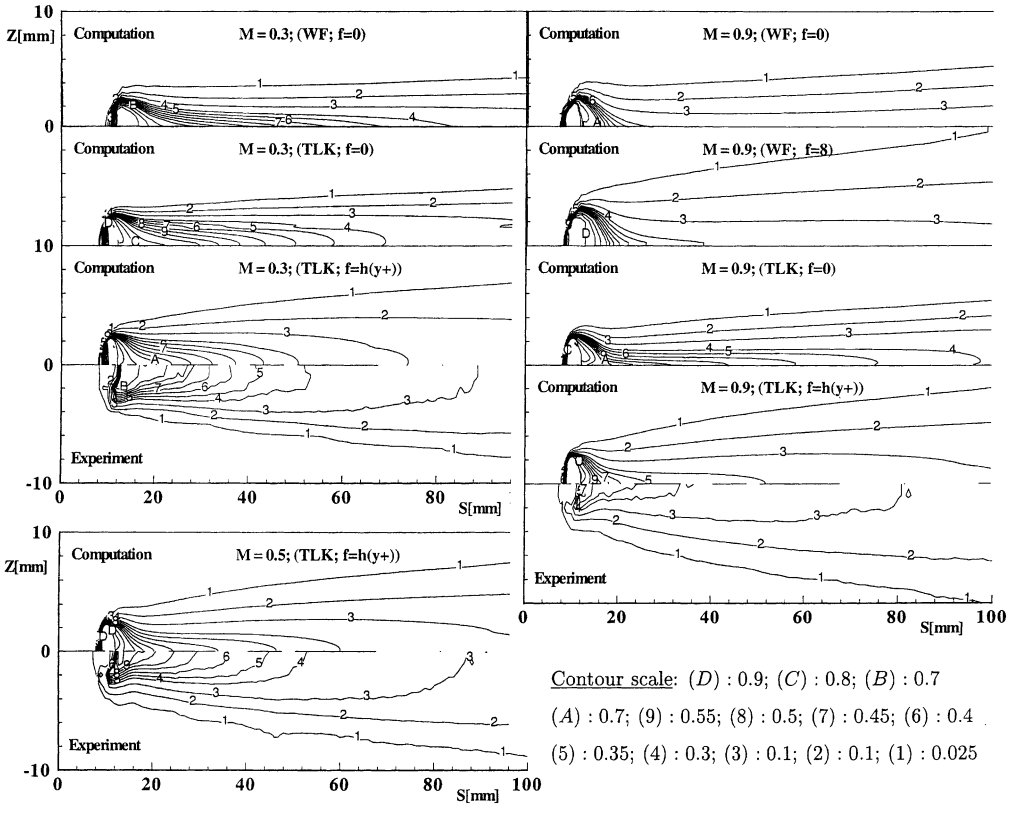

Fig. 5. Contours of film-cooling effectiveness for streamwise injection ($\gamma = 0°; M = 0.3, 0.5, 0.9$).

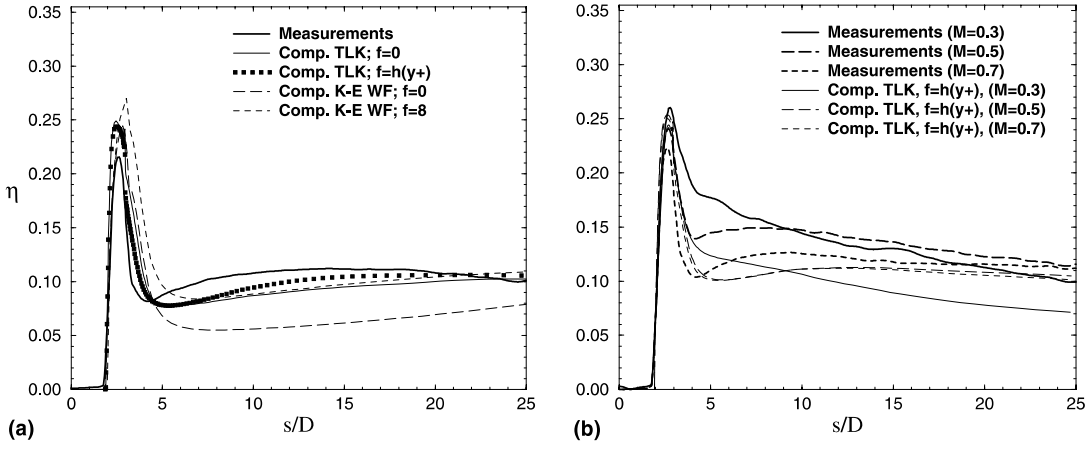

Fig. 6. Laterally averaged film-cooling effectiveness $\overline{\eta}$ for $\gamma = 0°$: (a) $M = 0.9$, various turbulence-model variants; (b) calculations with the two-layer model (TLK) and extended Bergeles correction for various M's.

good agreement obtained with the TLK without Bergeles correction ($f = 0$) for $\overline{\eta}$ is somewhat misleading and must be seen as the result of the compensation of η being predicted too high near the axis but not spreading sufficiently in the lateral direction (see Fig. 5). Fig. 6(b) shows the calculations obtained with the TLK and extended Bergeles correction for various blowing rates in comparison with experiments. It can be seen that the agreement is still rather good for $M = 0.7$ but deteriorates for smaller blowing rates where $\overline{\eta}$ is predicted to be too small, particularly right behind the injection. As mentioned already, this is a consequence of the fact that in the core region the higher η-values are restricted to a too narrow region in the calculations. The calculations with WFs show even larger deviations from the measurements for the low blowing rates (Rodi et al., 1997).

Finally, in Fig. 7 isotherms in the mid-plane of the injection hole as calculated with the TLK with extended Bergeles correction are compared with the corresponding isoconcentration lines deduced from the visualisation pictures taken in the experiments. There is fairly close qualitative similarity of the isotherms with the isoconcentration lines, showing that the bending-over of the discharged jet is predicted realistically.

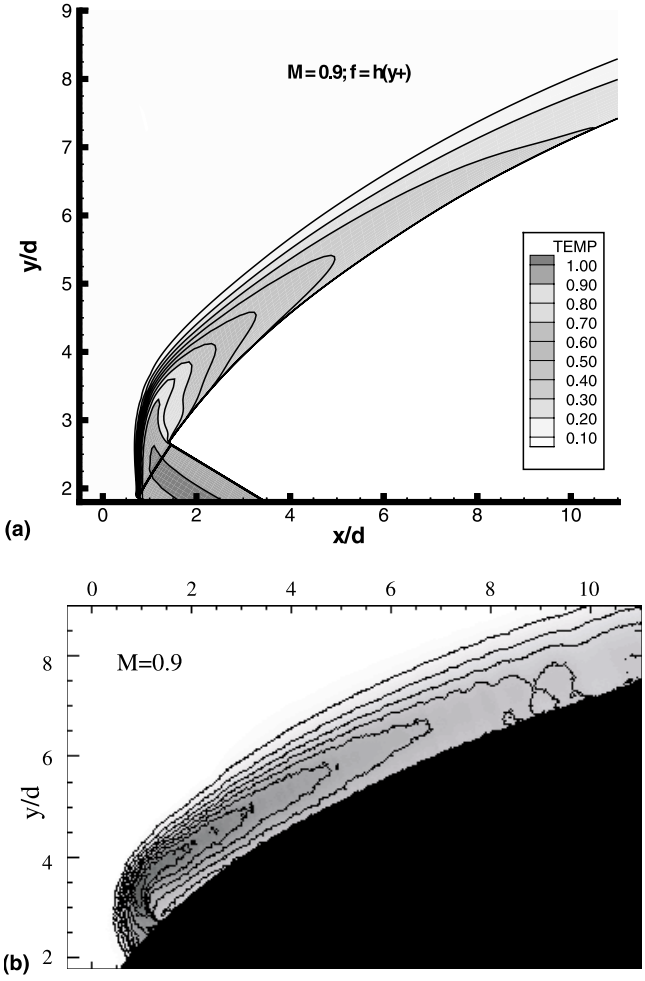

Fig. 7. Isotherms in mid-plane through injection hole for streamwise injection at $M = 0.9$: (a) calculations with TLK and Bergeles correction with $f = h(y^+)$; (b) from flow visualisation with air/oil–fog mixture.

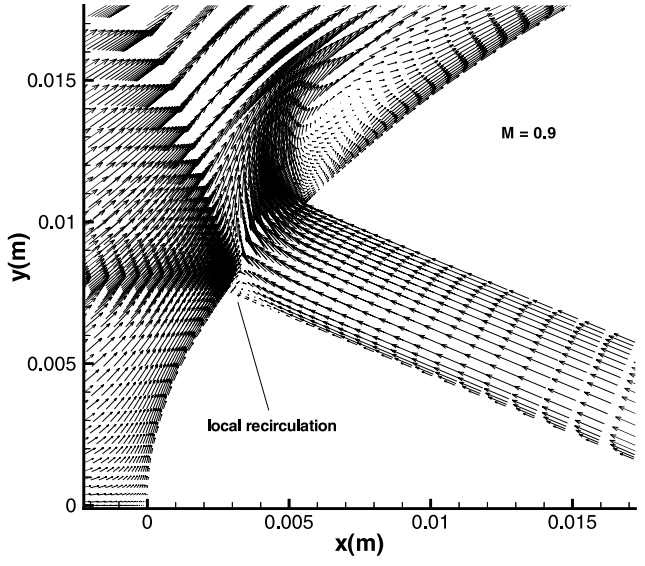

Fig. 8. Calculated velocity vectors in mid-plane through injection hole for lateral injection ($\gamma = 45°$); TLK model with Bergeles correction ($f = h(y^+)$).

5.2. Lateral injection ($\gamma = 45°$)

The lateral injection is under an angle of 45° to the x-axis. Fig. 8 displays the velocity vectors in the mid-plane through the hole for the blowing rate $M = 0.9$ as calculated with the TLK with extended Bergeles modification. At a low blowing rate of $M = 0.3$ (not shown), the jet again bends over quickly and there is only a thin reverse-flow region adjacent to the wall extending to about $0.9D$ downstream of the trailing edge of the injection hole. At the higher blowing rate of $M = 0.9$, the picture is quite different and also different from the flow establishing in the case of non-lateral injection (Fig. 4). Now the reverse flow underneath the bent-over jet develops more away from the wall; reverse flow near the wall occurs only down to about $0.15D$ from the trailing edge of the hole; beyond this point the near-wall flow has wall-jet behaviour which then develops into a boundary layer further downstream. For both blowing rates, the high near-wall resolution leads to the development of a local recirculation region inside the discharge channel near the leading edge of the injection hole.

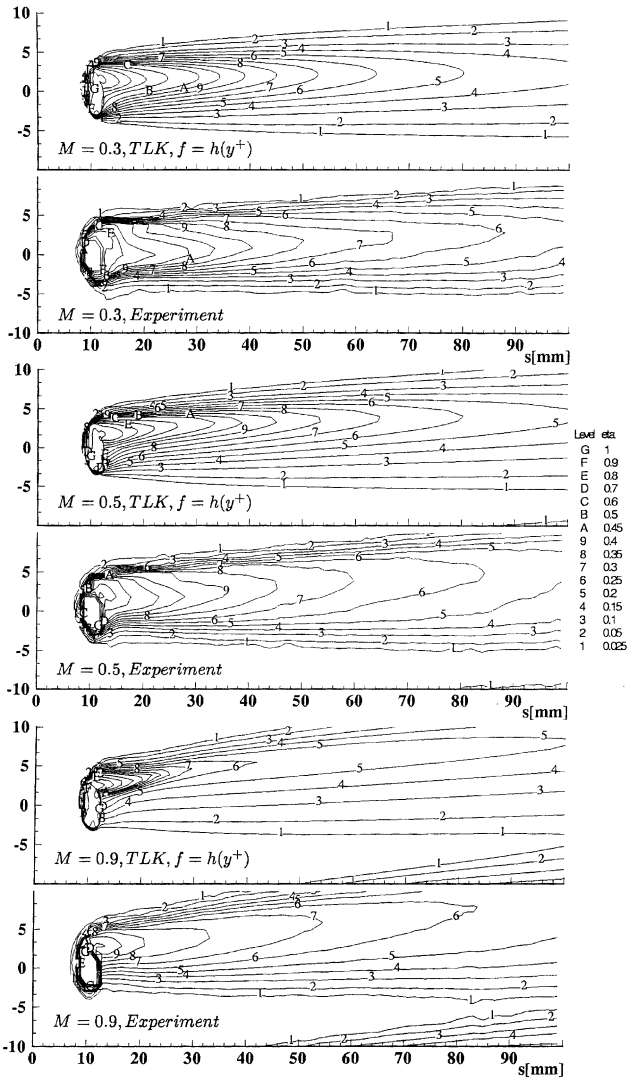

Fig. 9. Contours of film-cooling effectiveness for lateral injection ($\gamma = 45°$; $M = 0.3, 0.5, 0.9$).

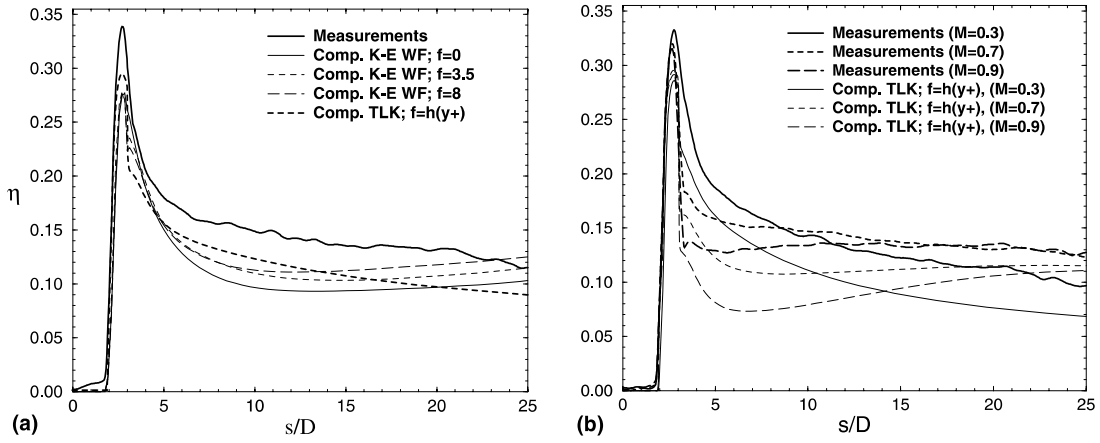

Fig. 10. Laterally averaged film-cooling effectiveness $\overline{\eta}$ for $\gamma = 45°$: (a) $M = 0.5$, various turbulence-model variants; (b) calculations with two-layer model (TLK) and extended Bergeles correction for various M's.

Fig. 9 compares the contours of the film cooling effectiveness η for the blowing rates $M = 0.3$, 0.5 and 0.9 as calculated with the TLK with extended Bergeles correction with the measurements. Also in this case, this model version gave the best results, the other versions yielding again too small lateral spreading of the temperature field (results are given in Rodi et al., 1997). As expected, in the case with lateral injection the contours are no longer symmetrical with respect to the $z = 0$ axis but are shifted in the direction of the injection. The trajectory of the jet, which runs along the peaks of each contour, is first inclined with respect to the $z = 0$ axis but further downstream runs approximately parallel to this axis. This behaviour is in general reproduced well by the calculations. For all blowing rates, the lateral spreading of the temperature field is calculated fairly correctly, but the axial decay of η in the core region is predicted too large so that the laterally averaged film cooling effectiveness $\overline{\eta}$ is too low (see Fig. 10). This is most serious for $M = 0.9$ at medium distances from the injection hole, while at larger distances the calculation approaches the measured $\overline{\eta}$ in this case.

Finally, Fig. 10 compares the calculated distributions of the laterally averaged film cooling effectiveness $\overline{\eta}$ with measurements. In (a), results obtained with various turbulence model variants are displayed for the blowing rate of $M = 0.5$. When using WFs without Bergeles correction, $\overline{\eta}$ is calculated to be too small especially near the discharge hole. When increasing the correction factor, an approach to the measured curve is obtained and the correct level is reached in the downstream region while in the intermediate region $\overline{\eta}$ is still too low. With the TLK and extended Bergeles correction, the correct shape of the distribution is predicted and altogether the results are the most realistic ones, but the level is somewhat underpredicted. Fig. 10(b) exhibits predictions for the blowing rates $M = 0.3$, 0.7 and 0.9 as obtained with the TLK with extended Bergeles correction. The figure shows that in the case with lateral injection, the agreement with the measurements improves with decreasing M, but the influence of M is always predicted correctly. For the higher blowing rates ($M = 0.7$, 0.9), $\overline{\eta}$ is significantly underpredicted in the intermediate region behind the injection hole but reaches levels close to the measured ones further downstream, as was explained above in connection with the contours.

6. Conclusions

Film cooling was calculated for a symmetrical model blade with lateral and streamwise cooling-air injection from one row of holes on each side placed near the leading edge. For various blowing rates, the flow and temperature fields around the blade and inside the injection channels was calculated with a flexible 3D finite-volume method on multi-block grids. Various versions of the k–ε turbulence model were used to simulate the turbulent momentum and heat exchange processes. These included the standard model with WFs bridging the viscous sublayer, a two-layer version resolving the viscous sublayer with a one-equation model and the Bergeles et al. (1978) anisotropy correction for enhancing the lateral exchange, the latter modified to account for the strong anisotropy of turbulence when the wall is approached in the viscous sublayer.

The flow field and its dependence on blowing rate and injection angle appear to be reasonably well predicted, with of course finer details resolved by the TLK. A quantitative validation of the velocity calculations was not possible due to the absence of measurements. However, for other situations like film cooling of a similar unsymmetrical blade (Theodoridis et al., 2000) and of a flat plate (Lakehal et al., 1998) a reasonable agreement with measurements was obtained for the flow field. The temperature field appears to be more difficult to predict. The basic evolution is simulated correctly and so are the influences of blowing rate and injection angle, but it is clear that the standard model with WFs severely underpredicts the lateral spreading of the temperature field. As a consequence, the laterally averaged film-cooling effectiveness is generally too low. The Bergeles anisotropy correction brings a significant improvement, but the best results are obtained when the adjustable parameter f is chosen twice as high as in the original Bergeles proposal. Resolving the near-wall zone brings by itself only little improvement, but when combined with an appropriately adjusted Bergeles correction for the anisotropy yields altogether a realistic lateral spreading and reasonably good results with regard to the contours of the film cooling effectiveness. On the other hand, the laterally averaged effectiveness could not be calculated in all cases with sufficient accuracy mainly due to an underprediction of the peak level of effectiveness and further refinement of the model appears necessary, perhaps accounting for the laminar–turbulent transition, which was so far neglected entirely, and also for curvature effects.

Acknowledgements

This work was sponsored by the German Federal Ministry of Education, Science, Research and Technology through

program TURBOTHERM under contract number 0326760D. The calculations were carried out on the *SNI S600/20* and *VPP 300/16* computers of the University of Karlsruhe.

References

AGARD Advisory Report 245, 1998. AGARD. Neuilly-sur-Seine, France.

Ardey, S., 1998. 3D Messung des Strömungsfeldes um die filmgekühlte Vorderkante einer Referenzschaufel. Abschlussbericht zum Turbotherm II Vorhaben 2.1.8.4, Universität der Bundeswehr, München.

Bergeles, G., Gosman, A.D., Launder, B.E., 1978. The turbulent jet in a cross stream at low injection rates: a three-dimensional numerical treatment. Numer. Heat Transfer 1, 217–242.

Bohn, D.E., Becker, V., Kusterer, K., Ardey, S., Fottner, L., 1997. The influence of slot injection and shower-head injection on the 3D flow field of a film-cooled turbine blade under consideration of side-wall effects. AIAA paper 97/7162.

Demuren, A.O., Rodi, W., Schönung, B., 1985. Systematic study of film cooling with a 3D calculation procedure. ASME paper 85-IGT-2.

Findlay, M.J., Salcudean, M., Gartshore, I.S., 1999. Jets in a crossflow – effects of geometry and blowing ratio. J. Fluids Eng. 121, 373–378.

Garg, V.K., 1999. Heat transfer on a film-cooled rotating blade using different turbulence models. Int. J. Heat Mass Transfer 42, 789–802.

Garg, V.K., Ameri, A.A., 1997. Comparison of two-equation turbulence models for prediction of heat transfer on film-cooled turbine blades. Numer. Heat Transfer, Part A 31, 347–371.

Garg, V.K., Rigby, D.L., 1999. Heat transfer on a film-cooled blade – effect of hole physics. Int. J. Heat Fluid Flow 20, 10–25.

Haslinger, W., Hennecke, D.K., 1997. High resolved distribution of adiabatic film cooling effectiveness for turbine leading edge film cooling. Paper ISABE 97-7113.

He, P., Salcudean, M., Gartshore, I.S., 1995. Computation of film cooling for the leading edge region of a turbine blade model. ASME paper 95-GT-20.

Honami, S., Shizawa, T., Uchiyama, A., 1992. Behaviors of the Laterally injected jet in film cooling: measurements of surface temperature and velocity/temperature field within the jet. ASME paper 92-GT-180.

Kohli, A., Bogart, D.G., 1995. Adiabatic effectiveness, thermal fields, and velocity fields for film cooling with large angle injection. ASME J. Turbomachinery 119, 352–358.

Lakehal, D., Theodoridis, G., Rodi, W., 1998. Computation of film cooling of a flat plate by lateral injection from a row of holes. Int. J. Heat Fluid Flow 19, 418–430.

Launder, B.E., Spalding, D.B., 1974. The numerical computation of turbulent flows. Comput. Meths. Appl. Mech. Eng. 3, 269–289.

Ligrani, P.M., Wigle, J.M., Jackson, S.W., 1994. Film-cooling from holes with compound angle orientations: Part 2 – Results downstream a single row of holes with 6d spanwise spacing. ASME J. Heat Transfer 116, 353–362.

Majumdar, S., Rodi, W., Zhu, J., 1992. Three-dimensional finite–volume method for incompressible flows with complex boundaries. J. Fluid Eng. 114, 496–503.

Martin, K.A., Thole, K.A., 1997. Leading edge film-cooling with compound angle injection. ASME paper 97-GT-297.

Norris, L.H., Reynolds, W.C., 1975. Turbulent channel flow with a moving wavy boundary. Rept. No. FM-10, Department of Mechanical Engineering, Stanford University.

Rhie, C.M., Chow, W.L., 1983. A numerical study of the turbulent flow past an isolated airfoil with trailing edge separation. AIAA J. 21, 1225–1532.

Rodi, W., 1991. Experience with two-layer models combining the k–ε model with a one-equation model near the wall. Paper AIAA-91-0216.

Rodi, W., Mansour, N.N., Michelassi, V., 1993. One-equation near-wall turbulence modeling with the aid of direct simulation data. J. Fluids Eng. 115, 196–205.

Rodi, W., Theodoridis G., Lakehal D., 1997. Entwicklung eines geeigneten Turbulenz- und Wärmeübergangsmodells für ein 3D Berechnungsverfahren der Filmkühlung an der Schaufelvorderkante. Abschlussbericht Institut für Hydromechanik, University of Karlsruhe, 141 pp.

Stone, H.L., 1968. Iterative solution of implicit approximations of multidimensional partial differential equations. SIAM J. Numer. Anal. 5, 530–558.

Theodoridis, G., Lakehal, D., Rodi, W., 2000. 3D calculations of the flow field around a turbine blade with film cooling injection near the leading edge, submitted.

Van Doormal, J.P., Raithby, G.D., 1984. Upstream weighted differencing schemes and their application to elliptic problems involving fluid flow. Comput. Fluids 2, 191–220.

Vogel, D.T., 1996. Numerische Untersuchung des Mischungsverhaltens von Filmkühlstrahlen in Turbinenströmungen. Dissertation, Ruhr-Universität Bochum.

Zhu, J., 1991. A low-diffusive and oscillating-free convective scheme. Commun. Appl. Numer. Meth. 7, 225–232.

Zhou, J.M., Salcudean, M., Gartshore, I.S., 1993. Prediction of film cooling by discrete hole injection. ASME paper 93-GT-75.